Spectrochimica Acta Part A: Molecular and Biomolecular Spectroscopy 323 (2024) 124882

Contents lists available at ScienceDirect

Spectrochimica Acta Part A: Molecular and Biomolecular Spectroscopy

journal homepage: www.journals.elsevier.com/spectrochimica-acta-part-a-molecular-and-biomolecular-spectroscopy

Thermoluminescence and ATR-FTIR study of UVC-irradiated low-density polyethylene (LDPE) food packaging

C. Boronat [a,b,*], V. Correcher [b], J.F. Benavente [b], J.C. Bravo-Yagüe [c]

[a] Department of Inorganic Chemistry, Faculty of Sciences, National University of Distance Education (UNED), Av. de Esparta s/n, 28232 Madrid, Spain
[b] Department of Environment, Centre for Energy, Environment and Technology Research (CIEMAT), Av. Complutense 40, 28040 Madrid, Spain
[c] Department of Analytical Sciences, Faculty of Sciences, National University of Distance Education (UNED), Av. de Esparta s/n, 28232 Madrid, Spain

HIGHLIGHTS

- Investigation of UVC radiation effects on LDPE food packaging samples.
- ATR-FTIR spectroscopy reveals LDPE degradation after UVC treatment.
- Chemical composition of the TLDs may influence UVC-TL response.
- TLDs exhibit intensity variations from photo-transferred luminescence (PTTL) process.
- The computerised glow curve deconvolution (CGCD) method estimates kinetic parameters.

GRAPHICAL ABSTRACT

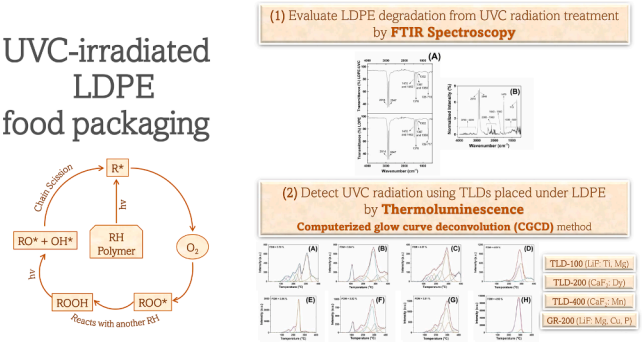

ARTICLE INFO

Keywords:
Low-density polyethylene
Ultraviolet C radiation
ATR-FTIR
Thermoluminescence
Kinetics analysis
Food packaging

ABSTRACT

This research aims to study the effects of ultraviolet C (UVC) radiation on low-density polyethylene (LDPE) food packaging. Main objectives include evaluating LDPE degradation and detecting UVC radiation using thermoluminescent dosimeters (TLDs) placed under LDPE samples. Results confirm accurate UVC detection after one hour of exposure, providing a useful tool for optimize food treatment procedures.

ATR-FTIR spectroscopy analysis revealed subtle alterations (<8 % transmittance relative) in UVC-irradiated LDPE samples, including possible C—H breakage (2910 and 2848 cm^{-1}) and potential —C═C— bond vibrations (1470 cm^{-1}), among others. However, observed variations may stem from LDPE properties rather than entirely from UVC radiation. A comparative study of UVC-induced thermoluminescence (TL) emissions provided insights into various TLDs materials. TL kinetic analysis, using computerised glow curve deconvolution (CGCD) method, unveiled trap charge activation due to UVC exposure, including partial ionization, bleaching effect and photo-transfer (PTTL) processes. LDPE samples amplified UVC-TL responses, revealing intensity differences between the TLDs attributed to the PTTL process, accentuated by the lack of an annealing treatment. Additionally, chemical composition of the TL detectors such as, type, concentration, number, oxidation states and ionic radii of their dopants may influence UVC-TL response. Consequently, TL intensity ratios follow as: GR-200 (LiF: Mg, Cu, P) > TLD-100 (LiF: Ti, Mg) > TLD-400 (CaF_2: Mn) > TLD-200 (CaF_2: Dy). Thus, GR-200 detects

* Corresponding author at: Department of Inorganic Chemistry, Faculty of Sciences, National University of Distance Education (UNED), Av. de Esparta s/n, 28232 Madrid, Spain.
E-mail address: cecilia.boronat@ccia.uned.es (C. Boronat).

https://doi.org/10.1016/j.saa.2024.124882
Received 22 April 2024; Received in revised form 18 July 2024; Accepted 23 July 2024
Available online 24 July 2024

ionizing radiation but cannot distinguish between ionizing and non-ionizing UVC radiation, while TLD-100 has limited effectiveness as a UVC radiation detector. In contrast, TLD-400 is suitable for detecting UVC radiation and TLD-200 emerges as the most favorable UVC detector, showing consistent response levels and minimal PTTL effect placed under the LDPE samples without the need of a thermal annealing treatment that makes the TLD-200 to be reusable in a low-cost measurement protocol.

1. Introduction

In the field of food preservation, ionizing radiation has demonstrated to be a versatile methodology, offering several applications to prolong the shelf life of products and guarantee food safety [1]. Techniques, including gamma-ray irradiation (utilizing isotopes such as ^{60}Co or ^{137}Cs), electron-beams (up to 10 MeV) and X-ray treatments (up to 7.5 MeV), have emerged as effective tools to conventional thermal and chemical preservation methods [1–3]. Recently, ultraviolet C (UVC) irradiation appears as an alternative to the aforementioned ionizing technique, giving rise to distinctive characteristics tailored for food preservation [4]. UVC radiation, with wavelengths ranging from 200 nm to 280 nm, exhibits germicidal properties by inducing DNA damage in microorganisms [4]. While commonly employed for air and water disinfection, its potential application in the food industry has got attention due to its ability to target surface contaminants on both food products and packaging materials [5–7].

Low-density polyethylene (LDPE) is a widely used material for food packaging due to its flexibility, transparency and moisture resistance [8,9]. Its versatile properties make it indispensable for packaging a diverse range of food products [10,11]. To prevent the risk of subsequent recontamination by microorganisms, food items used to be carefully prepackaged before being treated with irradiation. Hence, there is a scientific interest in investigating the UVC radiation effects on the intrinsic properties of packaging materials [12]. UVC irradiation of polymers can have various effects, including the generation of free radicals. This can lead to both cross-linking and scission of polymeric chains through a photo-oxidative degradation mechanism. When oxygen is present, this process may also result in the creation of low molecular weight radiolysis products and gases. Additionally, polymers commonly used in food packaging, which incorporate additives, are susceptible to degradation when exposed to irradiation. These degradation products have the potential to migrate into the food, affecting its toxicological safety and organoleptic properties. Both cross-linking and degradation processes can alter the optical and mechanical properties of these packaging materials [8]. While optimal cross-linking can improve mechanical strength and reduce permeability by forming a network, irradiated packaging materials might exhibit adverse optical properties such as colour changes or enhanced light transmission in the near UV spectrum. These changes could potentially impact the shelf life of the food [1,12,13].

Considering the effects of UVC radiation on polymers, especially LDPE food packaging material, it is essential to contemplate two fundamental aspects: (1) evaluating degradation of the polymer after UVC treatment and (2) detecting the presence of UVC on food items. To achieve these objectives, a comprehensive analysis could rely on two techniques: Fourier transform infrared spectroscopy (FTIR) and thermoluminescence (TL), respectively.

FTIR spectroscopy, employed to examine microscopic deformations and structural changes in polymers used for food packaging, provides valuable insights. This spectroscopic technique, reliant on the primary vibrational movements of structural groups in the polymer matrix, furnishes detailed molecular-level structural insights devoid of the requirement for physical or chemical sample preparation [9,14–16]. Moreover, it is essential to develop a technique capable of identifying food items subjected to UVC treatment. Such a methodology becomes indispensable for regulatory authorities, guaranteeing precise labelling and endorsing a standardised method to ascertain the total absorbed dose, in alignment with the EN 1788 standard procedure [17,18]. Detecting irradiated food by identifying alterations in its physical, chemical and biological characteristics is essential in this context [7,19,20]. Within this framework, TL emerges as a highly accurate, effective, suitable and cost-efficient method. TL involves the release of light from an insulator, semiconductor or dielectric solid when subjected to heat after ionizing or partially ionizing radiation exposure. Analytically heated, the TL signal is captured by a photomultiplier tube, concerning temperature or wavelength. And the resultant TL glow curve illustrates distinct luminescent patterns and intensity levels, indicative of the heating rate and radiation dosage absorbed [21].

Furthermore, UVC radiation can initiate a three-stage process closely associated with the luminescence mechanism [22]: (1) UVC radiation exhibits partial ionization, resulting in the partial release of electrons from molecules and atoms, consequently leading to bond dissociation as previously mentioned (i.e. photo-oxidation and photo-dissociation processes) [23]; (2) UVC radiation can initiate a bleaching effect or deactivate trapping sites [24]; and (3) UVC radiation can facilitate photo-transfer of charges from deeper to shallower traps, a phenomenon known as photo-transferred luminescence (PTTL) [25]. The PTTL emission observed from a material is intricately correlated with its UV-TL glow curve, which has undergone prior exposure to ionizing or partially radiation. This exposure induces the generation of free charges, subsequently captured within corresponding localised states. During following heating, electrons are thermally liberated from shallower traps and then recombine radiatively at luminescent centres. This process leads to the manifestation of the PTTL signal [25].

TL phosphors, such as TLD-100 (LiF: Ti, Mg), TLD-200 (CaF_2: Mn), TLD-400 (CaF_2: Dy) and GR-200 (LiF: Mg, Cu, P) could act as UVC detectors [7,22]. These materials achieve the requirements for ionizing and partially ionizing radiation detectors, as previously demonstrated [7,22]. Specifically, they are thermally and chemically stable, reusable without compromising the stability of their TL signals, exhibit a TL response that is reasonably independent of radiation energy, and are cost-effective [7,22].

Consequently, TL analysis allows for the determination of their compositions, genetic properties, structures and typomorphic characteristics, where extrinsic, structural, intrinsic and surface defects play crucial roles in generating distinct luminescence emissions. The location of the TL glow peak corresponds to a particular defect; nonetheless, slight changes in the lattice crystallinity structure order, for example, can cause nuanced shifts in the positions of their intensities and wavebands [26].

The mechanism involving the liberation of electrons from traps to recombine with holes and the emitted photons is governed by kinetic parameters associated with the defects mentioned earlier: activation energy (E), order of kinetics (b) and frequency factor (S). This parameters can be estimated using several methods, varying with the intricacy of the experimental TL glow curve, for example, isothermal decay (ID), peak shape (PS), initial rise (IR), variable heating rate (VHR) or computerised glow curve deconvolution (CGCD). Thus, simple TL curves consisting of a single maximum or separate maxima (i.e. groups of components without overlapping), can be analysed by: ID, or phosphorescence decay, where the glow emission is measured on irradiated samples at a constant temperature (T) just below the position of the TL maximum for a given time (t); one can determine E, S and b associated with the decay rate of the trapped electrons from a $\ln (I/I_0)$ vs t plot [27]; PS allows measuring E of a peak from the position of the maximum and

the widths or half-width intensity temperatures on both sides of the maximum temperature at the peak; *b* value can be directly calculated from the peak shape [28]; IR method estimates the *E* value from the initial rise *T* region of the TL glow curve, determined by the slope of a *Ln I* vs *1/T* Arrhenius plot. One of the main deficiencies of IR is its failure to consider luminescence efficiency, which encompasses both the probability of non-radiative and radiative transitions (i.e. the *E* value estimation using the IR method was previously undervalued compared to the actual activation energy). IR assumes that *E* value is independent of *b* and *S* [29]; VHR is based on the release of the electrons at different heating rates where the TL maxima shift towards higher temperatures as the HR increases and the glow intensity used to decrease. The ln (T_M^2/β) vs $1/k{\cdot}T_M$ Arrhenius plot allows us the estimation of *E* and *S* (from the straight line of E/k slope and the y-axis intercept respectively); VHR does not depend on the *b* value [30]. The assessment of the kinetic parameters of complex TL curves, which often involve overlapping components, can be effectively determined by CGCD method, widely recognized for calculating *E*, *S*, *b*, initial or concentration of trapped electrons [31]. CGCD enables the detailed deconvolution of intricate TL glow curves, allowing for precise identification and quantification of individual trapping states and recombination centres within TL materials such as TLD-100, TLD-200, TLD-400 and GR-200, all of which serve as UV-TL emission detectors [7,22]. The functions describing TL kinetics processes are assumed to follow first, second, mixed or general order kinetics [31]. Recently, a simplified methodology to examine TL glow curves while considering non-specific recombination-retrapping rates has been described [32].

This work describes the effect of UVC radiation on TL detectors positioned under LDPE food packaging samples of 0.01 mm considering: (1) evaluate LDPE degradation induced by UVC treatment using ATR-FTIR spectroscopy, and (2) confirm UVC radiation by assessing their UVC-TL responses through the polymer. Additionally, this study examines the changes in the physical–chemical processes within the phosphors exposed to UVC radiation based on the determination of kinetic parameters by means of the CGCD method.

2. Materials and methods

2.1. Experimental measurements on LDPE food packaging sample

This study focuses on an LDPE food packaging sample of 0.01 mm thickness, which was randomly acquired from a grocery store. The characterization of the LDPE sample was conducted employing ATR-FTIR spectroscopy technique, and the spectra were collected at room temperature (RT) from 4000 to 400 cm^{-1}, utilizing a Spectrum FT-IR-4100 spectrometer. The experimental equipment was precisely controlled using the JASCO Spectra Manager® software, with the spectral resolution at 4 cm^{-1}. UVC exposure was applied for one hour at RT through an automated irradiator designed at CIEMAT [33]. This device facilitated UVC radiation with a TUV-6 W Hg lamp (254.7 nm), with an irradiance of 0.03 $W{\cdot}m^{-2}$ at a distance of 10 cm. UVC radiation measurements were conducted using TLDs furnished by Harshaw Chemical Company. These materials, available in three types −LiF: Ti, Mg (TLD-100), CaF_2: Dy (TLD-200) and CaF_2: Mn (TLD-400) −each measuring 0.32 × 0.32 × 0.09 cm^3, served as detectors for UVC radiation. Additionally, discs of −LiF: Mg, Cu, P (GR-200) −from Beijing Shiying Radiation Detector Works were utilised, measuring 4.5 Ø 0.8 mm^3. These TLDs were positioned under the LDPE samples to assess radiation penetration during irradiation. After UVC irradiation, the TLDs underwent high-temperature treatment at 400 ± 1 °C for one hour in an electric oven, followed by annealing to eliminate any stored information. TL properties were analysed using an automated TL DA-12 Risø TL reader equipped with an EMI 9635 QA photomultiplier [34]. Emission analysis involved a FIB002-blue filter with a peak wavelength range of 320–480 nm (60 % of transmittance and FWHM of 80 ± 16 nm). The TL reader, equipped with a $^{90}Sr/^{90}Y$ source (rate of exposure at 0.011 $Gy{\cdot}s^{-1}$), underwent calibration using a photon source that included ^{137}Cs in a secondary standard laboratory [35]. To ensure accuracy, all TL readings were conducted with a linear heating rate of 5 $^{o}C{\cdot}s^{-1}$, spanning from RT up to 400 °C, in a N_2 atmosphere. Background signals originating from detector noise and incandescence were deduced from the TL data following a second TL readout of the TLDs, performed to confirm their values.

2.2. TL kinetic analysis using the CGCD method

The determination of the TL kinetic parameters, including −*E*− (activation energy, eV), −I_M− (intensity of the maximum, a.u.), −T_M− (temperature of the maximum, °C), −σ− (distribution wide, eV) and –*S*− (frequency factor, s^{-1}), from the observed TL glow curves was conducted using CGCD method [36]. This involved employing a linear combination of functions as presented in Eq. (1):

$$I\left(T_j\right) = \sum_{n=1}^{N_{peaks}} f_{(n)}\left(T_j; I_M^{(n)}, T_M^{(n)}, E^{(n)}, \sigma^{(n)}\right) \tag{1}$$

Acknowledging the principles of first order kinetics (FOK), the function $f_{(n)}\left(T_j; T_M^{(n)}, E, \sigma\right)$ is derived following the expression in Eq. (2), presuming $\sigma = 0.0$ eV (limited trap distribution).

$$f\left(T_j; I_M, T_M, E\right) = I_M \hat{\cdot} exp\left(\frac{E}{K_b \hat{\cdot} T_M} - \frac{E}{K \hat{\cdot} T_j}\right) \hat{\cdot} exp\left\{\frac{E}{K_b \hat{\cdot} T_M^2} \cdot \int_{T_M}^{T} e^{\frac{E}{K_b \hat{\cdot} T \cdot T_M} - \frac{E}{K_b \hat{\cdot} T \cdot T'}} \cdot dT'\right\} \tag{2}$$

Furthermore, Eq. (3) is established with $\sigma > 0.0$ eV (contemplating a continuous trap distribution).

$$f\left(T_j; I_M, T_M, E, \sigma\right) = I_M \frac{\int_{E_{0+7\hat{\cdot}\sigma}}^{E_2} g(E) \hat{\cdot} e^{\frac{-E}{K_b \hat{\cdot} T}} \hat{\cdot} exp\left\{\frac{E_0}{K_b \hat{\cdot} T_M} \hat{\cdot} e^{\frac{-E_0}{K_b \hat{\cdot} T_M}} \int_{T_0}^{T} e^{-\frac{E}{K_b \hat{\cdot} T'}} \cdot dT'\right\} dE}{\int_{E_1}^{E_2} g(E) \hat{\cdot} e^{\frac{-E}{K_b \hat{\cdot} T_M}} \hat{\cdot} exp\left\{\frac{E_0}{K_b \hat{\cdot} T_M} \hat{\cdot} e^{\frac{-E_0}{K_b \hat{\cdot} T_M}} \int_{T_0}^{T_M} e^{-\frac{E}{K_b \hat{\cdot} T'}} \cdot dT'\right\} dE} \tag{3}$$

Here, $g\ (E)$ is associated with a trap contribution distribution, factoring an exponential distribution as denoted Eq. (4).

$$g(E) = \frac{1}{\sigma} e^{-\frac{E-E_0}{\sigma}} \tag{4}$$

Glow curve fitting in the experimental data was achieved through an iterative approach utilizing the Levenberg–Marquardt algorithm, aiming to minimize the X^2, as defined in Eq. (5).

$$X^2 = \sum_{j=1}^{N_p} \left[I_j - \sum_{n=1}^{N_{peaks}} f_{(n)}\left(T_j; I_M^{(n)}, T_M^{(n)}, E^{(n)}, \sigma^{(n)}\right)\right]^2 = \sum_{j=1}^{N_p} \left[I_j - I(T_j)\right]^2 \tag{5}$$

where I_j aligns with the experimental data.

The frequency factor −*S*− is determined by Eq. (6).

$$S\left(s^{-1}\right) = \frac{\beta \hat{\cdot} E}{K_b \hat{\cdot} T^2{}_M} \hat{\cdot} e^{\frac{E}{K_b \hat{\cdot} T_M}} \tag{6}$$

where $\beta = 5$ °C/s is the heating rate and $K_b = 8.61 \cdot 10^{-5}$ eV/K is the Boltzmann constant.

3. Results and discussion

3.1. ATR-FTIR characterization

FTIR analysis characterize the degradation within the LDPE food packaging samples after UVC irradiation, giving information about

molecular alterations by analysing the functional groups present in the polymer. It identifies subtle changes in chemical bonds, including cross-linking, chain scission and the appearance of novel functional groups. These insights provide a comprehensive understanding of the potential degradation mechanisms induced by UVC radiation in LDPE material. As appreciated in Fig. 1(A), LDPE, which derivates from ethylene as its primary monomer $(C_2H_4)_n$, represents a versatile thermoplastic polymer synthesized through polymerization processes:

The UVC irradiation of polymers can initiate a photo-oxidative degradation mechanism, Fig. 1(B), encompassing steps of initiation, propagation and termination, as presented in Table 1. This mechanism initiates with an initial decomposition reaction, generating alkyl radicals (R*) from the polymer macromolecules (RH), consequently causing polymer chain fragmentation primarily through C–H scissions. This is followed by a propagation step that generates peroxy (ROO*) and hydroperoxide (ROOH) radicals, which can further decompose into alkoxy radicals (RO*). These types of radicals either abstract hydrogen from the polymeric structure or undergo β-scission. The process culminates in a termination step, resulting in the formation of diverse carbonyl species (C═O), leading to the subsequent degradation of the polymer matrix. This degradation process often induces a reduction in molecular weight, consequently compromising the tensile and mechanical characteristics of the material [12,13].

Numerous studies have extensively delved into exploring the mechanisms of photo-degradation and photo-oxidative degradation in polymers [12,13,37]. Photo-degradation can manifest under anaerobic conditions, leading to either cross-linking or chain fragmentation, or under aerobic conditions, resulting in in photo-oxidative degradation. UV radiation, in combination with various catalysts alone or in synergy, is capable of instigating and accelerating this process, especially at heightened temperatures. Moreover, in the presence of atmospheric oxygen, UV radiation causes photo-degradation, inducing effects such as yellowing, cross-linking, bleaching effect, gradual hardening and chain breakage due to oxidation in polymers [12,13,37].

Thus, FTIR spectroscopy serves as a powerful tool to investigate the formation of novel chemical linkages and functional groups through the photo-oxidative degradation process of the LDPE samples, providing insights into the molecular alterations within the plastic material. An analysis of ATR-FTIR spectra was conducted, and the identified bands correspond to specific molecules and functional groups. Subsequently, non-irradiated LDPE sample was compared with the one exposed to 1-hour UVC irradiation, as illustrated in Fig. 2(A). Further normalization of responses was executed by normalizing the spectra against the band with the highest intensity. This approach facilitated the comparison of relative changes in band intensities due to UVC irradiation. Fig. 2(B) illustrates the intensity differences between the normalized spectra of irradiated and non-irradiated LDPE, providing a clear depiction of variations across all bands in the spectrum (in Normalized Intensity (%) units). Additionally, a comprehensive delineation of the ATR-FTIR bands is outlined in Table 2.

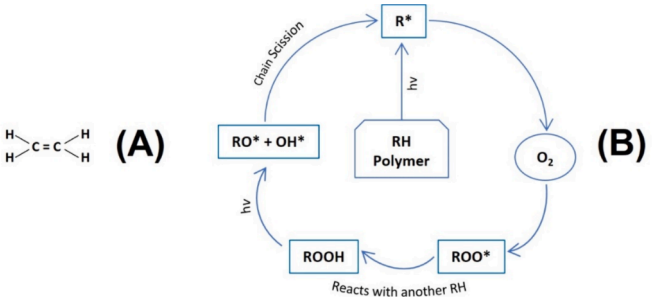

Fig. 1. (A) Molecular structure of low-density polyethylene $(C_2H_4)_n$. And (B) mechanism illustrating the photo-oxidative degradation of polymers (Figure adapted from [12]).

Table 1
Steps of the photo-oxidative degradation mechanism of polymers.

Step 1 – Initiation:	**RH (Polymer) → R***
Step 2 – Propagation:	**R* + O_2 → ROO*** **ROO* + RH → ROOH + R*** **ROOH → RO* + OH* → β-Scission**
Step 3 – Termination:	**2 ROO*** → Non radical products

The ATR-FTIR spectrum of LDPE samples, presented in Fig. 2(A), exhibits peaks at: 2914 and 2847 cm^{-1}, might be due to CH_2 asymmetric and symmetric stretching vibrations, respectively; 1470 and 1463 cm^{-1}, may suggest bending deformation and —C═C— stretching vibrations; 1376 cm^{-1}, could be linked to CH_3 symmetric deformation vibrations in the umbrella mode; 1367 and 1350 cm^{-1}, might be associated with wagging deformation vibrations; 1302 cm^{-1}, may correspond to twisting deformation vibrations and 729 and 717 cm^{-1}, could be due to CH_2 rocking deformation vibrations [14,16,38,39].

The normalized ATR-FTIR spectra of the non-irradiated LDPE sample –Fig. 2(A)– and the one exposed to 1-hour UVC irradiation –Fig. 2(B)– reveal a transmittance difference of less than 8 % compared to the average value after UVC exposure. The bands most affected were associated with CH_2 asymmetric and symmetric stretching vibrations (2914 and 2847 cm^{-1}), bending deformation and —C═C— stretching vibrations (1470 cm^{-1}) and CH_2 rocking deformation (715 cm^{-1}), which are characteristic of the molecular structure of LDPE $(C_2H_4)_n$. Nevertheless, the assessment of the photo-oxidative degradation process focuses on specific regions within the infrared spectrum, particularly related to the stretching vibrations of hydroperoxide (ROOH) radicals, peroxy (ROO*) radicals, carbonyl (C═O) and unsaturated groups (i.e., vinyl and vinylidene groups). Based on the literature [38,40–42], the intensity of these groups is known to increase with exposure time, serving as an indicator of material degradation. The absence of those bands in the present study underscores the resistance of the LDPE ATR-FTIR spectra under UVC radiation, suggesting their resilience against further degradation.

Thus, possible changes observed in the ATR-FTIR spectra of the LDPE material upon exposure to UVC irradiation may affect the following groups: bands peaking from 3700 to 3200 cm^{-1} may align with atmospheric water lines [43] and could also be attributed to the O—H stretching vibrations of hydroperoxides and alcohols, which result from the photo-oxidative degradation process [38,40–42]. The possible breakage of C—H bonds within the polymer chain results in alterations in both the intensity and position of CH_2 asymmetric (2910 cm^{-1}) and symmetric (2848 cm^{-1}) stretching bands [16,38,39]. Additionally, the spectral region between 2360 to 1960 cm^{-1}, could be associated with atmospheric water and CO_2 vibrational bands [43]. The carbonyl (C═O) region, peaking between 1780–1700 cm^{-1}, remains largely unaffected, contradicting literature that suggests alterations in these bands due to photo-oxidative degradation of polymer chains, caused by the presence of multiple functional groups. Some studies propose that the configuration of this band might correspond to the simultaneous presence of more than one functional group absorbing within the carbonyl region [38,40–42]. Specifically, various functional groups might contribute to this composite peak: vibrations from carboxylic acid groups (about 1708 cm^{-1}), ketones (around 1719 cm^{-1}), aldehydes (approximately 1738 cm^{-1}) and esters (around 1747 cm^{-1}), all related to carbonyl groups [42,44]. The appearance of a new band at 1640 cm^{-1} could potentially signify a consequence of the olefinic band [41]. The bands linked to the bending deformation and stretching of —C═C— bond vibrations peaked at 1470 cm^{-1} might undergo changes UVC irradiation, potentially resulting in the creation of new functional groups [38]. The spectral bands in the peroxide (ROO) region, peaking between 1325 to 1050 cm^{-1}, show minimal alterations. This contradicts the proposed

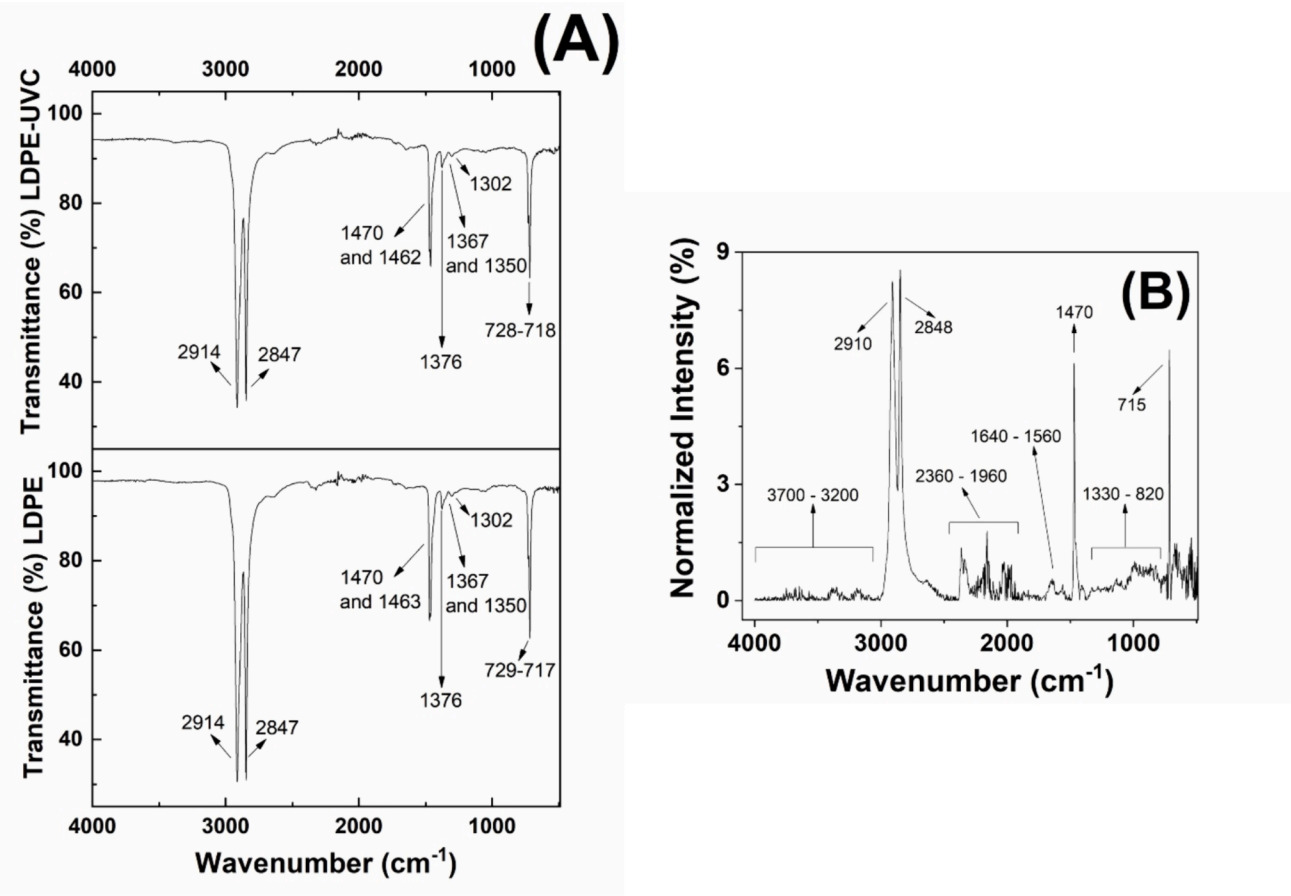

Fig. 2. (A) ATR-FTIR spectra of non-irradiated and 1-hour UVC irradiated LDPE food packaging samples. And (B) intensity differences between the normalized spectra of irradiated and non-irradiated LDPE food packaging samples.

Table 2
Vibrational modes associated with LDPE food packaging sample ATR-FTIR bands.

Wavenumber (cm^{-1})	Vibrational modes
2914	CH_2 asymmetric stretching
2847	CH_2 symmetric stretching
1470 and 1463	Bending deformation and stretching —C═C— bond
1376	CH_3 symmetric deformation (umbrella mode)
1367 and 1350	Wagging deformation
1302	Twisting deformation
729 and 717	CH_2 rocking deformation

alterations in these bands attributed to the photo-oxidative degradation of polymer chains in previous studies [42]. The photo-oxidation of ketones can lead to the generation of unsaturated groups, such us vinyl and vinylidene groups observed at 909 cm^{-1} and 888 cm^{-1}, respectively [40,42]. And UVC radiation can influence the crystalline structure of the polymer, causing changes in bands associated with the crystalline structure, particularly those in the 715 cm^{-1} region [45], which are attributed to CH_2 rocking deformation vibrations [16,38,39].

Therefore, the normalized ATR-FTIR spectra of LDPE samples in Fig. 2(B) suggest subtle alterations (<8 % transmittance relative) in the characteristic bands of LDPE material (CH_2 and —C═C— bonds). These observations imply that the LDPE sample exhibits minimal degradation after UVC treatment, as indicated by the following measurements. The minimal variances appear to arise from various aspects of the LDPE material, such as molecular mass distribution, crystalline matrix, additives, as well as potential factors like manufacturing procedures, storage practices, prior environmental exposure, among others. These factors collectively contribute to the observed differences rather than entirely being attributed to UVC treatment.

3.2. UVC-TL emissions in TLDs detectors

The TLDs materials, were used to detect UVC radiation [7,22] passing through the LDPE samples, potentially affecting packaged food items. This approach enables the discernment of irradiated LDPE food packaging samples, thereby guaranteeing the safety and quality of food items.

Exposing these detectors to UVC radiation reveals distinct variations in the UV-blue TL emission (Fig. 3), directly influenced by the characteristics of the UVC radiation source, including partial ionization, bleaching effect and photo-transfer processes. While TLDs demonstrate acceptable sensitivity to radiation with clearly defined peaks, each detector presents glow curves that differ significantly in intensity and shape due to the diverse structures and types of dopants employed. This variability can be systematically studied using the CGCD method, wherein the TL glow curve consists of individual peaks associated with specific trapping centres. To examine the physical–chemical mechanisms inherent in TL glow curves, it is necessary to analyse the curve into its individual glow peaks. Due to their complexity, these peaks are commonly modelled based on first-order kinetics.

As depicted in Fig. 3, the deconvolution analysis of UVC-irradiated TLDs without plastic samples and those under LDPE food packaging samples reveals distinct groups of components: eight for the TLD-100 –Fig. 3(A and E)– and TLD-200 –Fig. 3(B and F)–, nine for the TLD-400 –Fig. 3(C and G)– and five for the GR-200 –Fig. 3(D and H)–. Furthermore, the disparity in the relative intensity increases between

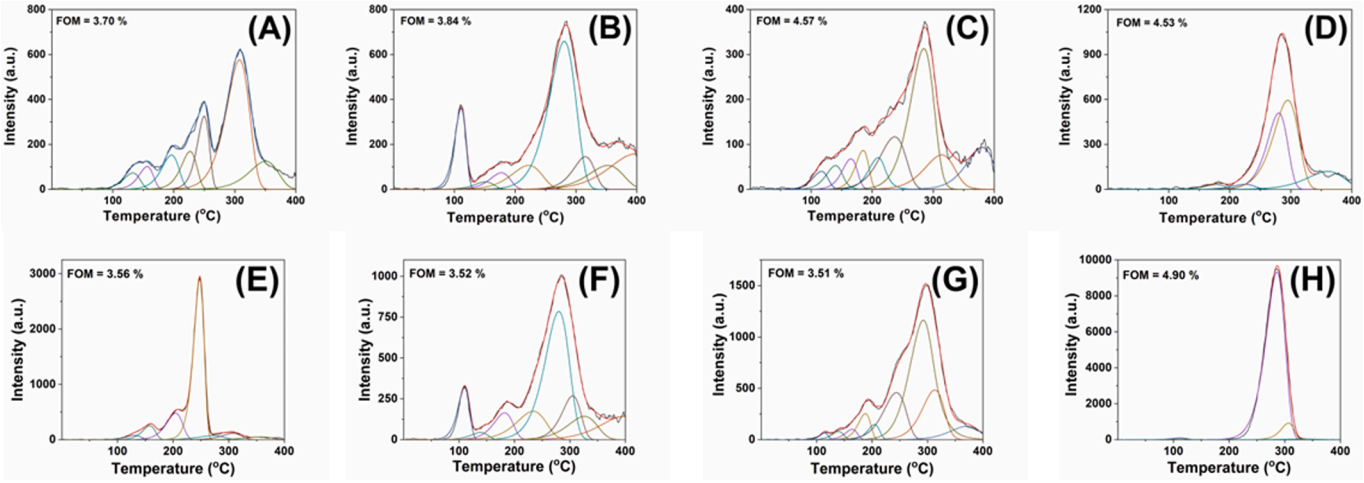

Fig. 3. Deconvolution of 1-hour UVC-induced TL glow emissions assuming First Order Kinetics (FOK) from TLDs detectors. Thus, (A) TLD-100, (B) TLD-200, (C) TLD-400 and (D) GR-200 emissions are shown without polymer; while (E) TLD-100, (F) TLD-200, (G) TLD-400 and (H) GR-200 emissions are depicted under LDPE food packaging samples. The Figure of Merit (FOM) ranges from 3.51 % to 4.90 %.

the UVC-TL emissions of the TLDs without plastic sample (1st line of the Fig. 3) and those under the LDPE material (2nd line of the Fig. 3) could be associated with the presence of a PTTL process. This process facilitates the migration of deep traps to shallower levels above 400 °C, enhancing the TL response and resulting in higher TL emission intensity compared to samples without plastic.

Additionally, GR-200 (Fig. 3H) demonstrates elevated intensity levels compared to TLD-100 (Fig. 3E), followed by TLD-400 (Fig. 3G) and TLD-200 (Fig. 3F), all positioned under LDPE food packaging samples. As previously noticed, these disparities in intensity may be linked to a PTTL process, which is facilitated by the absence of annealing treatment. In this study, annealing was not conducted, despite being a standard procedure to enhance detector performance after repeated use, thereby saving time and resources. Consequently, traps at higher temperatures exhibit increased occupancy in the absence of annealing. Upon exposure to UVC radiation, PTTL phenomenon preferentially facilitates the migration of charge carriers from deeper to shallower traps, thereby resulting in enhanced TL responses in detectors positioned under LDPE samples. This effect, regarding the difference in intensity ratio, is particularly pronounced in GR-200 (1:10), TLD-100 (1:5) and TLD-400 (1:4), whereas TLD-200 exhibits a nearly equal proportion.

TL emission is susceptible to influence from various factors related to defects within the material, encompassing intrinsic, structural, surface and extrinsic defects. These defects may induce fluctuations in the crystalline lattice structure, leading to subtle changes in both the position and intensity of emitted wavebands associated with the TL glow peak. Moreover, the TL response could be significantly influenced by the chemical composition of the TLDs, including the type and concentration of dopants, alongside their oxidation states and ionic radii. Dopants introduce energy levels within the band gap, thereby modulating trap depth and consequently shifting the position of the TL glow peak. Variations in chemical composition and dopant concentration can induce notable shifts in TL emission intensity and spectral characteristics. Additionally, factors such as crystalline structure, defect density and annealing treatment also exert considerable influence over the TL response. Specifically, the concentration of dopants could play a crucial role, where higher concentrations typically result in increased TL signal intensity due to enhanced electron trapping efficiency. However, excessively high concentrations may lead to increased carrier recombination, potentially reducing TL signal effectiveness. The size of dopants, characterised by their ionic radii, may affect the formation of electron traps within the material, where larger ionic radii might tend to generate deeper traps emitting TL light at higher temperatures, whereas smaller radii form shallower traps emitting light at lower temperatures. Lastly, the oxidation states of dopants could impact the energy levels involved in charge capture and release processes, thereby affecting TL signal characteristics such as peak temperature, peak shape and relative intensity.

Thus, both GR-200 and TLD-100 utilize a LiF matrix characterised by a simple cubic lattice structure (halite type), and their behaviour closely aligns with previous findings from beta source irradiation study [22]. The main difference between both materials lies in their dopant composition, while GR-200 (Fig. 3H) incorporates additional dopants (Mg, Cu, P) with multiple oxidation states, TLD-100 (Fig. 3E) relies on fewer dopants (Mg, Ti) with their respective oxidation states.

The Mg dopant typically assumes an oxidation state of +2 within the LiF matrix of both materials (GR-200 and TLD-100). This Mg^{2+} ion exhibits various coordination states, each with its own ionic radius, including IV (0.57 Å), V (0.66 Å), VI (0.72 Å) and VIII (0.89 Å). However, the predominant coordination state is VI (0.72 Å), favoured due to the octahedral arrangement provided by the LiF crystalline structure, where Mg^{2+} is surrounded by six fluoride ions, maximizing structural stability [46]. The Cu dopant predominantly exists in the oxidation state of Cu^{1+} with coordination states of II (0.46 Å), IV (0.6 Å) and VI (0.77 Å). However, when in the form of Cu^{2+}, coordination states IV (0.57 Å), V (0.65 Å) and VI (0.73 Å) are common, with IV and V being the most prevalent. It can form tetrahedral, trigonal bipyramidal and/or octahedral coordination structures, depending on the specific chemical environment of the GR-200 matrix. Cu^{3+} (low spin) is a less common oxidation state with coordination VI (0.54 Å) [46]. Within the GR-200 material, the P dopant is also present, predominantly existing in oxidation states of +3 and +5. The prevalent coordination state for P^{3+} oxidation is VI (0.44 Å), while coordination IV (0.17 Å), along with coordinations V (0.29 Å) and VI (0.38 Å), are also common for P^{5+} oxidation [46]. It can form coordination structures in the LiF lattice that could be tetrahedral and/or octahedral. Conversely, the Ti dopant is primarily found in the +4 oxidation state in the TLD-100 matrix, with coordination VI (0.605 Å) being predominant, forming an octahedral structure. This dopant can exhibit oxidation states of +2, +3 and +4. For Ti^{2+}, coordination VI (0.86 Å) is typical, while coordination VI (0.67 Å) is common for Ti^{3+}. Additionally, Ti^{4+} can adopt various coordination states, including IV (0.42 Å), V (0.51 Å), VI (0.605 Å), and VIII (0.74 Å) [46].

The enhanced UVC-TL response observed in the GR-200 material (Fig. 3H), when compared to other detectors like TLD-100 (Fig. 3E) and placed under LDPE, can be attributed to its doping with multiple elements exhibiting various oxidation states (such as Mg^{2+}, $Cu^{1+,2+,+3}$ and $P^{3+,5+}$), along with their larger ionic radii. This diversity in oxidation

states expands the possibilities of coordination and the formation of radiation traps. Additionally, this variation results in GR-200 detector (Fig. 3H) displaying the most significant intensity difference (with a 10x intensity ratio), possibly due to the previously discussed PTTL process. Enhanced electron-trapping capacity, resulting from an increased number of dopants and their respective oxidation states, could significantly contribute to an increase in defects (i.e. extrinsic and structural, among others), leading to a higher UVC-TL response in the GR-200 material. In summary, the presence of more dopant elements and the variety of their oxidation states in the GR-200 could contribute to a greater intensification of the UVC-TL response when placed under the LDPE sample (Fig. 3H), suggesting higher sensitivity of the detector under practical application conditions. However, the GR-200 material may require subsequent annealing treatment to facilitate trap evacuation at higher temperatures and allow for material recycling, although this entails increased time and cost investment.

On the other hand, both TLD-400 and TLD-200 utilize a CaF_2 matrix characterised by a face-centred cubic lattice structure (fluorite type). In this case, the behaviour of both detectors closely resembles that observed in previous research following UVC irradiation [22]. Despite sharing the same number of dopants, they differ in type and oxidation states. Specifically, TLD-400 (Fig. 3G) incorporates Mn with a greater number of oxidation states, whereas TLD-200 (Fig. 3F) contains Dy with a single oxidation state.

In the TLD-400 material, the Mn dopant exhibits multiple oxidation states, consisting of +2, +3, +4, +5, +6 and +7. Mn^{2+} typically adopts a coordination number of VI (0.83 Å), forming octahedral complexes with various ligands. The ionic radius of Mn^{2+} varies depending on its coordination environment, typically ranging from approximately 0.66 Å to 0.96 Å (from IV to VIII). In the case of Mn^{3+}, it can also adopt a coordination number of VI, forming octahedral complexes similar to Mn^{2+}. In this oxidation state, the ionic radius of Mn^{3+} is generally around 0.58 Å (low spin) and 0.645 Å (high spin). Conversely, Mn^{4+} can have coordination numbers of IV (0.39 Å) and VI (0.53 Å), forming tetrahedral complexes. Moreover, Mn^{5+} can exist in coordination number IV (0.33 Å). Additionally, manganese can exist in higher oxidation states such as Mn^{6+} and Mn^{7+}, but these are less common and typically involve coordination numbers and ionic radii that vary depending on the specific chemical environment [46]. Thus, Mn^{2+} is a transition metal ion with a $3d^5$ electron configuration, known for its strong interaction with the crystal field, particularly in $d \rightarrow d$ transitions. According to the literature [47,48], Mn^{2+} ions occupying Ca^{2+} sites emit light at 578 nm, corresponding to the yellow-green spectral emission, attributed to the $^4T_2(G) \rightarrow {}^6A_1(S)$ transition. In contrast, the Dy dopant typically exists as Dy^{3+}, which can adopt various coordination environments, including VI (0.912 Å), VII (0.97 Å), VIII (1.027 Å) and IX (1.083 Å). Among these, coordination VI (0.912 Å) is the most prevalent in the CaF_2 matrix of the TLD-200 due to its higher stability and occurrence frequency [46]. The emission of light from Dy^{3+} ions result through electric and magnetic dipole transitions within the 4*f* electron orbitals or $4f^{n-1}$ and 5*d* hybridization states. The 5*s* and 5*p* orbitals shield the *f* electrons, resulting in sharp emissions. Despite *f*–*f* transitions being prohibited by selection rules in lanthanide ions, the crystal field surrounding the Dy^{3+} ion can weaken these rules, allowing luminescence even at RT. Peaks in the Dy^{3+} absorption spectrum correspond to specific colours, including blue at 450 nm–490 nm ($^4F_{9/2} \rightarrow {}^6H_{15/2}$), yellow-green at 540 nm–580 nm ($^4F_{9/2} \rightarrow {}^6H_{13/2}$), red at 650 nm–665 nm ($^4F_{9/2} \rightarrow {}^6H_{11/2}$) and red-IR at 730 nm–775 nm ($^4F_{9/2} \rightarrow {}^4F_{11/2} + {}^6H_{9/2}$). These transitions originate from the ground state of free Dy^{3+} ions. Thus, the Dy^{3+} spectrum shows two main emission bands: the blue band ($^4F_{9/2} \rightarrow {}^6H_{15/2}$), resulting from a magnetic dipole transition relatively insensitive to the crystal field, and the yellow-green band ($^4F_{9/2} \rightarrow {}^6H_{13/2}$), which critically depends on the crystal field environment and is dominant at low symmetry sites. Conversely, at high symmetry sites, the blue emission tends to be stronger than the yellow-green emission [48,49].

As seen in Fig. 3G, the disparity in UVC-TL signal intensity in the presence of plastic is more notable for TLD-400 (with a 4x intensity ratio) compared to TLD-200 (Fig. 3F), despite both materials sharing the same CaF_2 matrix and dopant quantity. The presence of Mn with multiple oxidation states ($Mn^{2+,3+,4+,5+,6+,7+}$) and coordination environments in the TLD-400 material might contribute to its luminescence properties and influences its TL response to UVC radiation exposure [46]. This increased electron-trapping capacity and the higher number of oxidation states of the Mn dopant in TLD-400 (Fig. 3G) could enhance its TL response compared to the TLD-200 detector (Fig. 3F), where Dy^{3+} has a single oxidation state, resulting in fewer involved electrons and fewer traps within the lattice. Additionally, TLD-400 exhibits a more pronounced intensity difference, which may also be attributed to the aforementioned PTTL process.

Thus, the concentration, number and type of dopants seem to have a significant influence on the TL response, possibly having more impact than the number of oxidation states and their corresponding ionic radii, which depend on coordination states. Consequently, the number of dopants could be a primary determinant of detector TL response due to a PTTL process without an annealing treatment. For example, GR-200, with three dopants, shows higher TL response intensity than TLD-100, which has two dopants. Even when the number of dopants is the same, variations in the number of oxidation states and ionic radii may still play a role. This could explain why TLD-400 demonstrates a higher difference in intensity compared to TLD-200. This observation underscores the importance of dopant quantity in optimizing detector sensitivity and performance. However, further investigation is needed to confirm such assertion.

In addition, Table 3 presents the TL kinetic parameters of the TLDs both without plastic samples and those placed under the LDPE samples. The TLD-100 reveals the activation of three traps at temperatures over ~270 °C, with activation energies of 1.12, 1.69 and 1.50 eV. When positioned under the LDPE sample, peak 4 (at ~230 °C) seems to be masked by the intensity differences between peaks 3 and 5. Peak 3 (at ~200 °C) intensifies threefold, possibly due to photo-oxidation process, while peak 5 (at ~250 °C) emerges as the predominant peak (with a ninefold increase), which may be linked to the PTTL process. Similarly, the TLD-200 appears to share identical traps irrespective of the presence of LDPE food packaging sample, within the temperature range of ~130 °C to 240 °C, with activation energies of 0.94, 1.02 and 0.81 eV. Additionally, UVC radiation on the TLD-400 activates low-temperature traps (T < 200 °C), resulting in a complex structure comprised of nine groups of components, with less presence of the PTTL effect in its signal (i.e., peak 8 at ~310 °C with a sixfold increase in intensity). Conversely, the GR-200 exhibits negligible TL emission up to ~200 °C, displaying five maxima. And the preferred positions of peaks 3 (at ~290 °C, with x18 intensity ratio) and peak 4 (at ~310 °C) could be associated with the PTTL process. The T_M (°C) is correlated with the E (eV), S (s^{-1}) and β ($s^{-1} \cdot {}^{o}C$), and besides, the E parameter could be associated with the width of each peak (while maintaining the asymmetry characteristic of the FOK method). This suggests that wider maxima are observable at higher temperatures with activation energy values lower than those peaks occurring at lower temperatures.

3.2.1. UVC-TL emission in TLD-100 (LiF: Ti, Mg) detector

As depicted in Fig. 3(E), the UVC-TL emission in the TLD-100 detector under the LDPE food packaging sample can be categorised into:

The range of lower temperatures (<270 °C), the TL glow emission exhibits four individual peaks centred at ~130 °C (peak 1), ~160 °C (peak 2), ~200 °C (peak 3) and ~250 °C (peak 5). The shape of these peaks suggests a first-order kinetics process [22], and the absence of peak 4 could be attributed to its masking by the relative intensity differences caused by peaks 3 and 5. This might indicate the presence of different phenomena in both peaks. For instance, the photo-oxidation process may occur in peak 3 (~200 °C), which exhibits a threefold increase in intensity under the LDPE sample (481 a.u.). Additionally, the PTTL process contributes to the appearance of the most intense peak 5

Table 3
TL kinetic parameters of the TLDs detectors without and under LDPE food packaging samples after one hour of UVC irradiation.

		Without LDPE				Under LDPE			
	Peak n°	**E** (eV)	**I_M** (a.u.)	**T_M** (°C)	**S** (s^{-1})	**E** (eV)	**I_M** (a.u.)	**T_M** (°C)	**S** (s^{-1})
TLD-100	1	1.05	74	133	$3.58{\cdot}10^{12}$	1.04	78	131	$4.02{\cdot}10^{12}$
	2	1.35	102	156	$2.59{\cdot}10^{15}$	1.37	251	158	$4.56{\cdot}10^{15}$
	3	1.33	153	196	$7.25{\cdot}10^{13}$	1.35	481	205	$5.50{\cdot}10^{13}$
	4	1.69	169	227	$3.75{\cdot}10^{16}$	–	–	–	–
	5	2.37	326	250	$3.35{\cdot}10^{22}$	2.52	2912	248	$1.34{\cdot}10^{24}$
	6	–	–	–	–	1.12	73	272	$5.11{\cdot}10^{9}$
	7	1.51	577	308	$2.96{\cdot}10^{12}$	1.69	114	308	$1.21{\cdot}10^{14}$
	8	1.38	125	351	$3.12{\cdot}10^{10}$	1.50	49	357	$2.27{\cdot}10^{11}$
TLD-200	1	1.37	362	111	$5.44{\cdot}10^{17}$	1.23	319	110	$7.41{\cdot}10^{15}$
	2	0.96	34	151	$7.20{\cdot}10^{10}$	0.94	44	139	$1.11{\cdot}10^{11}$
	3	1.03	74	177	$9.92{\cdot}10^{10}$	1.02	164	182	$4.94{\cdot}10^{10}$
	4	0.82	107	222	$4.34{\cdot}10^{7}$	0.81	174	234	$1.96{\cdot}10^{7}$
	5	1.18	659	281	$1.16{\cdot}10^{10}$	1.18	785	280	$1.15{\cdot}10^{10}$
	6	1.69	145	316	$8.69{\cdot}10^{13}$	1.68	268	305	$1.35{\cdot}10^{14}$
	7	1.14	106	353	$2.60{\cdot}10^{8}$	1.14	143	326	$6.85{\cdot}10^{8}$
	8	0.98	158	397	$3.02{\cdot}10^{6}$	0.98	143	397	$2.82{\cdot}10^{6}$
TLD-400	1	1.12	39	113	$1.79{\cdot}10^{14}$	1.90	65	113	$4.99{\cdot}10^{24}$
	2	1.21	49	134	$4.39{\cdot}10^{14}$	1.51	77	137	$1.73{\cdot}10^{18}$
	3	1.44	66	162	$2.08{\cdot}10^{16}$	1.60	99	162	$1.74{\cdot}10^{18}$
	4	1.77	87	184	$1.39{\cdot}10^{19}$	1.74	254	188	$5.20{\cdot}10^{18}$
	5	1.68	62	202	$2.47{\cdot}10^{17}$	2.01	144	202	$1.06{\cdot}10^{21}$
	6	1.07	117	236	$9.68{\cdot}10^{9}$	1.18	455	241	$9.78{\cdot}10^{10}$
	7	1.45	306	280	$4.08{\cdot}10^{12}$	1.48	995	279	$8.94{\cdot}10^{12}$
	8	1.28	73	306	$2.95{\cdot}10^{10}$	1.57	473	308	$1.05{\cdot}10^{13}$
	9	1.70	93	379	$3.08{\cdot}10^{12}$	1.38	131	369	$1.35{\cdot}10^{10}$
GR-200	1	1.06	33	178	$2.35{\cdot}10^{11}$	–	–	–	–
	2	1.13	33	225	$1.74{\cdot}10^{11}$	–	–	–	–
	3	1.56	510	280	$5.20{\cdot}10^{13}$	1.56	9332	286	$3.73{\cdot}10^{13}$
	4	1.33	596	295	$1.53{\cdot}10^{11}$	2.48	922	307	$1.43{\cdot}10^{21}$
	5	1.06	120	361	$5.09{\cdot}10^{7}$	0.89	32	333	$3.87{\cdot}10^{6}$

(at ~250 °C), as previously explained. This peak is almost nine times more intense for the TLD-100 under LDPE –Fig. 3(E)– (2912 a.u.) than without the plastic sample –Fig. 3(A)– (326 a.u.), indicating the potential involvement of the PTTL process. These four peaks are likely related to the ionizing part, potentially originating from the generation of Ti^{4+}–OH^- defect complexes alongside Mg^{2+} vacancies, referred to as Mg-dipoles. Additionally, they may be linked to Ti^{4+}–OH^-/Mg^{2+}-trimer defect complexes and/or Mg^{2+} dipoles [50]. The presence of OH^- ions in the LiF matrix of the TLD-100 (with an ionic radius of 1.37 Å) has been established, and previous studies have shown the substitution of F^- ions with an ionic radius of 1.33 Å. These OH^- groups exhibit favorable reactions with metals in the TLD-100 detector, comprising Ti^{4+} and Mg^{2+} ions. Consequently, an enhancement in the OH^- ions concentration could intensify TL sensitivity [51].

And, at higher temperatures (>270 °C) primarily corresponds to the non-ionizing part. In this context, two TL emission peaks are observed at ~310 °C (peak 7) and ~360 °C (peak 8), while peak 6 (at ~270 °C) could be partially ionizing as it represents the frontier between both components of UVC radiation. All of these peaks demonstrate behaviour of first-order kinetics, suggesting that the TL process engages identical traps in the range of RT-270 °C (i.e., the defects are the same) [22].

Additionally, TLD-100 without plastic sample (–Fig. 3(A)–) displays enhanced sensitivity to UVC radiation, as indicated by the signal at ~310 °C (peak 7), linked to the non-ionizing UVC part (5:1). Conversely, the TLD-100 under the LDPE sample (–Fig. 3(E)–) demonstrates reduced sensitivity to the non-ionizing aspect around ~310 °C, with a ratio of 1:2:1. This phenomenon could suggest that the LDPE material selectively absorbs the non-ionizing UVC part while allowing penetration of the ionizing component. For such reason, the TLD-100 does not prove to be an effective detector for UVC radiation under this LDPE food packaging sample.

3.2.2. *UVC-TL emission in TLD-200 (CaF_2: Dy) detector*

The UVC-TL emission from the TLD-200 detector positioned under the LDPE food packaging sample (–Fig. 3(F)–) reveal emissions that can be related to structural defects and impurities caused by Dy^{3+} ions, which possess atomic radii of 1.59 Å and occupy the Ca^{2+} sites (1.74 Å) in the CaF_2 matrix [22], where:

The peak 1, observed at a lower temperature (~110 °C), demonstrates higher sensitivity to ionizing radiation [22].

The three TL emission peaks, observed at ~140 °C (peak 2), ~ 180 °C (peak 3) and ~235 °C (peak 4), could be due to the bleaching effect of UVC radiation on the TL signal [22].

Conversely, peaks observed at ~280 °C (peak 5), ~310 °C (peak 6), ~330 °C (peak 7) and ~400 °C (peak 8) might be directly related to the ionizing part of UVC [22]. Additionally, the kinetic order for TLD-200 material is variable and intricately influenced by the duration of annealing treatment [52]. This variability is attributed to the continuous distribution of traps associated with the detector.

The presence of the plastic sample leads to differences in the temperature range from approximately 130 °C to 240 °C (from peaks 2 to 4), which are associated with the non-ionizing part, leading to ratios of 1:2:3 and 1:4:4, respectively. However, there are no discernible fluctuations in intensity values between TLD-200 without the plastic sample –Fig. 3(B)– and under the LDPE sample –Fig. 3(F)–, indicating minimal PTTL effect in this detector. For instance, the most intense peak 5 at ~280 °C shows a nearly equal intensity ratio between both samples. As a result, this detector requires no annealing treatment to facilitate trap emptying at high temperatures (above 400 °C). By omitting this posterior treatment, the detector can be reused, leading to substantial time and cost savings. For such reason, and consistently exhibiting response levels (1:4:4) from ~130 °C to 240 °C (correlated with the non-ionizing part), the efficacy of TLD-200 in detecting UVC radiation is confirmed.

3.2.3. UVC-TL emission in TLD-400 (CaF_2: Mn) detector

The UVC-TL emission from the TLD-400 detector positioned under the LDPE food packaging sample (−Fig. 3(G)−), can be classified into:

TL emissions up to ~200 °C (from peak 1 to 5), which could be linked to UVC radiation [22]. The intensity ratios for TLD-400 without the plastic sample (−Fig. 3(C)−) and under the LDPE sample (−Fig. 3(G)−) for the non-ionizing part show a slightly higher sensitivity.

And a wide maximum at approximately 290 °C that can be deconvoluted into four components centred at ~240 °C (peak 6), ~280 °C (peak 7), ~310 °C (peak 8) and ~370 °C (peak 9), associated with the ionizing part. These emissions could also be linked to Mn^{2+} impurities and structural defects present in Ca^{2+} positions in the CaF_2 matrix, with atomic radii of 1.17 Å and 1.74 Å, respectively [53]. According to the literature, this complex TL curve might not be analysed presuming the model grounded in the discrete trap distribution, thus suggesting the T_m-T_{stop} method denotes the existence of closely overlapping components likely correlated with a continuum in the trap distribution [53].

The UVC-TL glow curve with the LDPE sample displays an increase in the ionizing component of these signals (3:8:4:1) compared to the TLD-400 without the plastic sample (2:4:1:1), possibly due to the ability of the LDPE sample to transmit the ionizing part. This TL enhancement could be associated with the presence of the PTTL process. Meanwhile, the non-ionizing aspect shows slightly elevated sensitivity to UVC radiation in relation to the TLD-400 without the plastic sample. As a result, TLD-400 could be deemed suitable for detecting UVC radiation, given its capability to exhibit a TL signal reaching 200 °C.

3.2.4. UVC-TL emission in GR-200 (LiF: Mg, Cu, P) detector

The UVC-TL emission of the LDPE food packaging sample on the GR-200 detector is presented in Fig. 3(H). The primary signal peaks around 290 °C (peak 3), potentially stemming from the ionizing part [22]. This emission is likely due to the recombination of crystalline imperfections, such as H-F defects (colour centres in the LiF crystal matrix) and $V_k - e$ centres (electron traps and vacancies) [54]. The sensitivity to the ionizing aspect becomes evident at around 300 °C (from peaks 3 to 5), with a minimal response up to approximately 230 °C (peaks 1 and 2). According to the literature [55], this peak follows first-order kinetics according to CGCD method.

The UVC-TL glow curve of GR-200 (−Fig. 3(D)−) exhibits five peaks, where peak 1 is attributed to the non-ionizing part, while peaks from 2 to 5 are linked to the ionizing aspect. Conversely, the UVC-TL glow curve of the GR-200 placed under the LDPE sample (−Fig. 3(H)−), reveals three peaks linked to the ionizing part. It should be noted that peaks 1 and 2, observed at lower temperatures ($T < 200$ °C), exhibit temporal instability over time and cannot be considered peak maxima. Their presence may be attributed to prompt signal curves, indicative of the short time elapsed between irradiation-measurement processes. As previously discussed, the disparity in relative intensity between the UVC-TL emissions of GR-200 without a plastic sample and under the LDPE material could be associated with a PTTL process. This phenomenon can be observed in the enhanced UVC-TL emission of peak 3 (at ~290 °C, with x18 intensity ratio, reaching 9332 a.u.) and peak 4 (at ~310 °C, with 922 a.u.). This process facilitates the migration of deep traps to shallower levels above 400 °C, increasing the TL response and resulting in higher TL emission intensity compared to samples without plastic. This phenomenon is more pronounced in the GR-200 detector and could be addressed by an annealing treatment, which would imply a higher cost in terms of time and resources. Additionally, the LDPE sample demonstrates greater capabilities in transmitting the ionizing part of UVC radiation. Therefore, GR-200 shows promise as a viable option for detecting ionizing radiation, although it lacks the ability to differentiate between the ionizing and non-ionizing components of UVC radiation [22].

4. Conclusions

This study investigates the effects of UVC radiation treatment on LDPE food packaging samples. Our primary objectives include evaluating LDPE degradation and detecting UVC radiation using TLDs placed under LDPE samples, which is essential for optimizing food treatment procedures.

ATR-FTIR spectroscopy analysis revealed subtle alterations (<8 % transmittance relative) in UVC-irradiated LDPE food packaging samples. Specifically, UVC exposure could lead to: atmospheric water lines and O—H stretching vibrations peaking from 3700 to 3200 cm^{-1}, possible breakage of C—H bonds affecting CH_2 asymmetric (2910 cm^{-1}) and symmetric (2848 cm^{-1}) stretching bands, with the region between 2360 to 1960 cm^{-1} offering insights into atmospheric water and CO_2 vibrational bands; appearance of a new band at 1640 cm^{-1}, possibly due to the olefinic band; potential changes in bands associated with —C═C— bond vibrations at 1470 cm^{-1}, leading to the creation of new functional groups; generation of unsaturated groups, such as vinyl and vinylidene groups (909 cm^{-1} and 888 cm^{-1}, respectively), due to the photo-oxidation process; and UVC radiation may induce changes in bands associated with the crystalline structure of the polymer, particularly those at 715 cm^{-1} attributed to CH_2 rocking deformation vibrations. Additionally, the C═O stretching peak stability (1780−1700 cm^{-1}) suggests LDPE sample resilience to degradation when exposed to UVC radiation, with minimal alterations observed in spectral bands in the peroxide (ROO) region (1325 to 1050 cm^{-1}). These findings suggest minimal impact on the LDPE molecular structure from photo-oxidative degradation processes. Observed variations may stem from intrinsic LDPE properties, rather than entirely from UVC irradiation.

Furthermore, a comparative study of UVC-TL emissions among several TLDs materials provides valuable insights into their suitability for UVC radiation detection. The TL kinetic analysis, obtained through CGCD method, reveals the activation of trap charges induced by UVC exposure, attributed to partial ionization, bleaching effect and photo-transfer processes. The presence of LDPE food packaging samples amplified their UVC-TL response, with disparities in intensity observed between TLDs without and under LDPE material. This discrepancy suggests the involvement of a PTTL process, facilitated by the absence of annealing treatment. Specifically, GR-200 exhibits heightened intensity levels compared to TLD-100 detector under LDPE sample, owing to its doping with multiple elements possessing various oxidation states. Similarly, TLD-400 demonstrates superior UVC-TL response compared to TLD-200, despite both sharing the same CaF_2 matrix and dopant quantity, due to the presence of Mn with multiple oxidation states and coordination environments. Thus, chemical composition of the TLDs, such as type, concentration and number of dopants seem to have a significant influence on the TL response, potentially outweighing the influence of oxidation states and their ionic radii.

Based on their UVC-TL responses: GR-200 detects ionizing radiation but cannot distinguish between ionizing and non-ionizing UVC radiation. The difference in UVC-TL emission intensity under LDPE indicates a PTTL process, notably in peaks 3 and 4 (around 300 °C), involving deep trap migration above 400 °C to enhance TL response. Addressing this in GR-200 may necessitate annealing treatment, albeit with increased time and cost implications. The effectiveness of TLD-100 as a UVC radiation detector under LDPE food packaging is limited. Peak 3 exhibits a threefold intensity increase under LDPE, indicating photo-oxidation process. Additionally, the PTTL process intensifies peak 5 (around 250 °C) under LDPE compared to without plastic. TLD-400 would be a suitable UVC detector according to its TL signal up to around 200 °C, although it presents less PTTL process. And, TLD-200 emerges as the most favorable detector, displaying consistent response levels and minimal PTTL effect placed under the LDPE samples. This eliminates the need for a thermal annealing treatment, making TLD-200 reusable using a low-cost measurement protocol.

Funding

This research did not receive any specific grant from funding agencies in the public, commercial, or not-for-profit sectors.

CRediT authorship contribution statement

C. Boronat: Writing – review & editing, Writing – original draft, Investigation. **V. Correcher:** Writing – review & editing, Writing – original draft, Investigation. **J.F. Benavente:** Investigation. **J.C. Bravo-Yagüe:** Writing – review & editing, Writing – original draft, Investigation.

Declaration of competing interest

The authors declare that they have no known competing financial interests or personal relationships that could have appeared to influence the work reported in this paper.

Data availability

Data will be made available on request.

Acknowledgments

Cecilia Boronat would like to thank for the predoctoral researcher contract with UNED-SANTANDER, affiliated with the UNESCO Chair, and for the assistance provided through the program "*UNESCO Chair on Science and Innovation for Sustainable Development: Global Food Production and Safety*".

References

[1] A.G. Chmielewski, Radiation technologies: the future is today, Radiat. Phys. Chem. 213 (2023) 111233, https://doi.org/10.1016/j.radphyschem.2023.111233.
[2] S. Ghazala, Part 179—Irradiation in the Production, Processing and Handling of Food, first ed., The CRC Master Keyword Guide for Food, CRC Press, 2020, pp. 1054–1059, doi: 10.1201/9780203504529-58.
[3] N.D. Yordanov, Z. Pachova, Gamma-irradiated dry fruits: an example of a wide variety of long-time dependent EPR spectra, Spectrochim. Acta A Mol. Biomol. Spectrosc. 63 (2006) 891–895, https://doi.org/10.1016/j.saa.2005.10.023.
[4] M. Pacheco, J. Dikec, P. Winckler, C. Coelho, J.M. Perrier-Cornet, Spectroscopic and microscopic characterization of dipicolinic acid and its salt photoproducts – A UVc effect study on DPA in solution and in bacterial spores, Spectrochim. Acta A Mol. Biomol. Spectrosc. 280 (2022) 121502, https://doi.org/10.1016/j.saa.2022.121502.
[5] C. Jo, K.H. Lee, Comparison of the efficacy of gamma and UV irradiation in sanitization of fresh carrot juice, Radiat. Phys. Chem. 81 (2012) 1079–1081, https://doi.org/10.1016/j.radphyschem.2011.11.070.
[6] U. Prajapati, R. Asrey, E. Varghese, A.K. Singh, M. Pal Singh, Effects of postharvest ultraviolet-C treatment on shelf-life and quality of bitter gourd fruit during storage, Food Packag. Shelf Life 28 (2021) 100665, https://doi.org/10.1016/j.fpsl.2021.100665.
[7] C. Boronat, V. Correcher, J.C. Bravo-Yagüe, Detecting ultraviolet C radiation under polyethylene terephthalate (PET) packaging by thermoluminescence analysis using commercial dosimeters, Food Packag. Shelf Life 42 (2024) 101263, https://doi.org/10.1016/J.FPSL.2024.101263.
[8] S.M. Elghnam, Y.H. Abdelalim, M.A. Hamad, Influence of weathering exposure on UV light absorption in low density polyethylene LDPE grad-LA071, J. Mater. Res. Technol. 19 (2022) 1493–1496, https://doi.org/10.1016/j.jmrt.2022.05.096.
[9] A.A. Moez, S.S. Aly, Y.H. Elshaer, Effect of gamma radiation on low density polyethylene (LDPE) films: optical, dielectric and FTIR studies, Spectrochim. Acta A Mol. Biomol. Spectrosc. 93 (2012) 203–207, https://doi.org/10.1016/j.saa.2012.02.031.
[10] N.C. Bandyopadhyay, V. More, J. Tripathi, S. Gautam, Gamma radiation treatment to ensure microbial safety of ready to bake (RTB) vegetable toppings/fillers and retain their nutritional qualities during cold storage, Radiat. Phys. Chem. 176 (2020) 108939, https://doi.org/10.1016/j.radphyschem.2020.108939.
[11] S. Chytiri, A.E. Goulas, A. Badeka, K.A. Riganakos, D. Petridis, M.G. Kontominas, Determination of radiolysis products in gamma-irradiated multilayer barrier food packaging films containing a middle layer of recycled LDPE, Radiat. Phys. Chem. 77 (2008) 1039–1045, https://doi.org/10.1016/j.radphyschem.2008.04.007.
[12] E. Yousif, R. Haddad, Photodegradation and photostabilization of polymers, especially polystyrene: review, Springerplus 2 (2013) 398, https://doi.org/10.1186/2193-1801-2-398.
[13] A.L. Andrady, A.M. Heikkilä, K.K. Pandey, L.S. Bruckman, C.C. White, M. Zhu, L. Zhu, Effects of UV radiation on natural and synthetic materials, Photochem. Photobiol. Sci. 22 (2023) 1177–1202, https://doi.org/10.1007/s43630-023-00377-6.
[14] A.K. Chaudhary, S.P. Chitriv, K. Chaitanya, R.P. Vijayakumar, Influence of ultraviolet and chemical treatment on the biodegradation of low-density polyethylene and high-density polyethylene by Cephalosporium strain, Environ. Monit. Assess. 195 (2023) 395, https://doi.org/10.1007/s10661-023-10982-8.
[15] S.V. Kumar, B. Ghadei, S.K. Chaudhuri, J.B.M. Krishna, D. Das, A. Saha, Chemical transformations and changes in free volume holes in high-energy proton irradiated low-density polyethylene (LDPE), Radiat. Phys. Chem. 77 (2008) 751–756, https://doi.org/10.1016/j.radphyschem.2007.11.002.
[16] J.V. Gulmine, P.R. Janissek, H.M. Heise, L. Akcelrud, Polyethylene characterization by FTIR, Polym. Test. 21 (2002) 557–563, https://doi.org/10.1016/S0142-9418(01)00124-6.
[17] EN 1788, Thermoluminescence detection of irradiated food from which silicate minerals can be isolated. Retrieved from EN 1788 - English version Foodstuffs-Thermoluminescence detection of irradiated food from which silicate minerals can be i... (europa.eu), 2001 Accessed April 10, 2024. Belgium, European Committee for Standardization.
[18] J. Raffi, N.D. Yordanov, S. Chabane, L. Douifi, V. Gancheva, S. Ivanova, Identification of irradiation treatment of aromatic herbs, spices and fruits by electron paramagnetic resonance and thermoluminescence, Spectrochim. Acta A Mol. Biomol. Spectrosc. 56 (2000) 409–416, https://doi.org/10.1016/S1386-1425(99)00252-8.
[19] V. Correcher, J. Garcia-Guinea, Application of the EN 1788 European standard for the control of saffron, pepper and blends, Food Control 22 (2011) 173–179, https://doi.org/10.1016/j.foodcont.2010.05.020.
[20] V. Correcher, J. Garcia-Guinea, Potential use of the activation energy value calculated from the thermoluminescence glow curves to detect irradiated food, J. Radioanal. Nucl. Chem. 298 (2013) 821–825, https://doi.org/10.1007/s10967-013-2473-3.
[21] S.W.S. McKeever, Mechanisms of thermoluminescence production in materials for radiation dosimetry, Radiat. Prot. Dosim. 17 (1986) 431–435, https://doi.org/10.1093/oxfordjournals.rpd.a079854.
[22] C. Boronat, V. Correcher, J.C. Bravo-Yagüe, I. Sarasola-Martin, J. Garcia-Guinea, J. F. Benavente, Comparing the effect of electron beam, beta and ultraviolet C exposure on the luminescence emission of commercial dosimeters, Spectrochim. Acta A Mol. Biomol. Spectrosc. 295 (2023) 122571, https://doi.org/10.1016/J.SAA.2023.122571.
[23] V. Correcher, C. Boronat, M.D. Virgos, J. Garcia-Guinea, UV-induced thermoluminescence of natural Ca-Rich carbonates, J. Appl. Spectrosc. 86 (2020) 1004–1009, https://doi.org/10.1007/s10812-020-00931-5.
[24] M. Topaksu, V. Correcher, C. Boronat, J. Garcia-Guinea, Z.G. Portakal, S. Akça, UV effect on the cathodo- and thermoluminescence properties of a gem-quality Cr-rich diaspore (α-AlOOH), Appl. Radiat. Isot. 141 (2018) 101–106, https://doi.org/10.1016/j.apradiso.2018.08.025.
[25] E. Bulur, Photo-transferred luminescence from BeO ceramics, Radiat. Meas. 42 (2007) 334–340, https://doi.org/10.1016/j.radmeas.2007.02.065.
[26] V. Correcher, J. Garcia-Guinea, Cathodo- and photoluminescence emission of a natural Mg-Cr carbonate layered double hydroxide, Appl. Clay Sci. 161 (2018) 127–131, https://doi.org/10.1016/j.clay.2018.04.022.
[27] C.E. May, J.A. Partridge, Thermoluminescent kinetics of alpha-irradiated alkali halides, J. Chem. Phys. 40 (1964) 1401–1409, https://doi.org/10.1063/1.1725324.
[28] R. Chen, On the calculation of activation energies and frequency factors from glow curves, J. Appl. Phys. 40 (1969) 570–585, https://doi.org/10.1063/1.1657437.
[29] F. Aramu, P. Brovetto, A. Rucci, Activation energy in the NaCl thermoluminescence, Phys. Lett. 23 (1966) 308–309, https://doi.org/10.1016/0031-9163(66)90012-6.
[30] M. Topaksu, V. Correcher, J. Garcia-Guinea, M. Yüksel, Effect of heating rate on the thermoluminescence and thermal properties of natural ulexite, Appl. Radiat. Isot. 95 (2015) 222–225, https://doi.org/10.1016/j.apradiso.2014.10.020.
[31] G. Kitis, TL glow-curve deconvolution functions for various kinetic orders and continuous trap distribution: acceptance criteria for E and s values, J. Radioanal. Nucl. Chem. 247 (2001) 697–703, https://doi.org/10.1023/A:1010688122988.
[32] J.F. Benavente, J.M. Gómez-Ros, V. Correcher, A kinetic model for the thermoluminescent high dose response of LiF:Mg, Cu, P (MCP-N), Appl. Radiat. Isot. 170 (2021) 109634, https://doi.org/10.1016/j.apradiso.2021.109634.
[33] A. Delgado, V. Unamuno, J.L. Muñiz, V. Correcher, J.M. Gómez Ros, A simple UV irradiator for low dose reassessment with LiF TLD-100, Radiat. Prot. Dosim. 67 (1996) 303–306, https://doi.org/10.1093/oxfordjournals.rpd.a031834.
[34] L. Bøtter-Jensen, G.A.T. Duller, A new system for measuring optically stimulated luminescence from quartz samples, Int. J. Radiat. Appl. Instrum. D. Nucl. Tracks. Radiat. Meas. 20 (1992) 549–553, https://doi.org/10.1016/1359-0189(92)90003-E.
[35] V. Correcher, A. Delgado, On the use of natural quartz as transfer dosemeter in retrospective dosimetry, Radiat. Meas. 29 (1998) 411–414, https://doi.org/10.1016/S1350-4487(98)00040-7.
[36] J.F. Benavente, J.M. Gómez-Ros, A.M. Romero, Thermoluminescence glow curve deconvolution for discrete and continuous trap distributions, Appl. Radiat. Isot. 153 (2019) 108843, https://doi.org/10.1016/j.apradiso.2019.108843.
[37] A.P. Kumar, D. Depan, N. Singh Tomer, R.P. Singh, Nanoscale particles for polymer degradation and stabilization-Trends and future perspectives, Prog. Polym. Sci. 34 (2009) 479–515, https://doi.org/10.1016/j.progpolymsci.2009.01.002.

[38] T.S. Tofa, F. Ye, K.L. Kunjali, J. Dutta, Enhanced visible light photodegradation of microplastic fragments with plasmonic platinum/zinc oxide nanorod photocatalysts, Catalysts 9 (2019) 819, https://doi.org/10.3390/catal9100819.
[39] B.C. Smith, The infrared spectra of polymers III: hydrocarbon polymers, Spectroscopy 36 (11) (2021) 22–25, https://doi.org/10.56530/spectroscopy.mh7872q7.
[40] M. Gardette, A. Perthue, J.L. Gardette, T. Janecska, E. Földes, B. Pukánszky, S. Therias, Photo- and thermal-oxidation of polyethylene: comparison of mechanisms and influence of unsaturation content, Polym. Degrad. Stab. 98 (2013) 2383–2390, https://doi.org/10.1016/j.polymdegradstab.2013.07.017.
[41] H. Qin, C. Zhao, S. Zhang, G. Chen, M. Yang, Photo-oxidative degradation of polyethylene/montmorillonite nanocomposite, Polym. Degrad. Stab. 81 (2003) 497–500, https://doi.org/10.1016/S0141-3910(03)00136-8.
[42] T.S. Tofa, K.L. Kunjali, S. Paul, J. Dutta, Visible light photocatalytic degradation of microplastic residues with zinc oxide nanorods, Environ. Chem. Lett. 17 (2019) 1341–1346, https://doi.org/10.1007/s10311-019-00859-z.
[43] T. Hakkarainen, E. Mikkola, J. Laperre, F. Gensous, P. Fardell, Y. Le Tallec, C. Baiocchi, K. Paul, M. Simonson, C. Deleu, E. Metcalfe, Smoke gas analysis by Fourier transform infrared spectroscopy - summary of the SAFIR project results, Fire Mater. 24 (2000) 101–112, https://doi.org/10.1002/1099-1018(200003/04)24:2<101::AID-FAM729>3.0.CO;2-2.
[44] G. Socrates, Infrared and Raman Characteristic Group Frequencies. Tables and Charts, 2001.
[45] R. Caban, FTIR-ATR spectroscopic, thermal and microstructural studies on polypropylene-glass fiber composites, J. Mol. Struct. 1264 (2022) 133181, https://doi.org/10.1016/j.molstruc.2022.133181.
[46] R.D. Shannon, Revised effective ionic radii and systematic studies of interatomic distances in halides and chalcogenides, Acta Cryst. A 32 (1976) 751–767, https://doi.org/10.1107/S0567739476001551.
[47] J. Garcia-Guinea, V. Correcher, A. Quejido, A. Laiglesia, N. Can, The role of rare earth elements and Mn^{2+} point defects on the luminescence of bavenite, Talanta 65 (2005) 54–61, https://doi.org/10.1016/j.talanta.2004.05.016.
[48] V. Correcher, J. Garcia-Guinea, Characterization of the cathodoluminescence emission of kamphaugite-(Y) and kristiansenite from Spain, Phys. Chem. Miner. 47 (2020) 6, https://doi.org/10.1007/s00269-019-01071-9.
[49] C. Boronat, T. Rivera, J. Garcia-Guinea, V. Correcher, Cathodoluminescence emission of REE (Dy, Pr and Eu) doped $LaAlO_3$ phosphors, Radiat. Phys. Chem. 130 (2017) 236–242, https://doi.org/10.1016/j.radphyschem.2016.09.005.
[50] J.S. Dryden, B. Shuter, The dependence of the thermoluminescence of LiF: Mg^{2+} crystals on the state of aggregation of the Mg^{2+} ions, J. Phys. D Appl. Phys. 6 (1973) 123–130, https://doi.org/10.1088/0022-3727/6/1/316.
[51] D. Weiss, Y.S. Horowitz, L. Oster, Delocalized recombination kinetic modeling of the LiF:Mg, Ti (TLD-100) glow peak 5 TL system, Radiat. Meas. 43 (2008) 254–258, https://doi.org/10.1016/j.radmeas.2007.10.026.
[52] A.N. Yazici, M. Bedir, A.S. Sökücü, The analysis of dosimetric thermoluminescent glow peak of CaF_2: Mn after β-irradiation, Nucl. Instrum. Methods. Phys. Res. B. 259 (2007) 955–965, https://doi.org/10.1016/j.nimb.2007.02.104.
[53] M. Topaksu, V. Correcher, J. Garcia-Guinea, Luminescence emission of natural fluorite and synthetic CaF_2: Mn (TLD-400), Radiat. Phys. Chem. 119 (2016) 151–156, https://doi.org/10.1016/j.radphyschem.2015.10.002.
[54] B. Yang, L. Wang, P.D. Townsend, H. Gao, Comparison between the low temperature thermoluminescence spectra in annealed LiF:Mg, Cu, LiF:Mg, Cu, P and LiF:Mg, Cu, Si, Nucl. Instrum. Methods. Phys. Res. B. 266 (2008) 2581–2586, https://doi.org/10.1016/j.nimb.2008.03.199.
[55] Y.S. Horowitz, M. Moscovitch, Highlights and pitfalls of 20 years of application of computerised glow curve analysis to thermoluminescence research and dosimetry, Radiat. Prot. Dosim. 153 (2013) 1–22, https://doi.org/10.1093/rpd/ncs242.